Molecular Insight into the Structure and Dynamics of $LiTf_2N$/Deep Eutectic Solvent: An Electrolyte for Li-ion Batteries

Kishant Kumar[a,*], Anand Bharti[b], Rudra Kumar[c]

[a] *Department of Chemical Engineering, National Institute of Technology Warangal, Warangal, Telangana, India–506004*
[b] *Department of Chemical Engineering, Birla Institute of Technology Mesra, Ranchi, Jharkhand, India–835215*
[c] *EIC Sustainable and Civil Technologies, Tecnológico de Monterrey, Monterrey, N.L., 64849, Mexico*

Abstract

Two choline based deep eutectic solvent namely ethaline and glyceline have been used in different applications such as metal extraction, solubility and in electrochemistry because of its easy availability, inexpensive and non-toxic nature. In this work, molecular dynamics simulation was employed to study the structural and transport properties of ethaline and glyceline when blended with Li^+ based salt (Lithium Bis (trifluoromethane sulfonyl) imide ($LiTf_2N$)) in varying concentration for the application as electrolytes in lithium ion batteries. The effect of varying temperature and concentration on the structural and transport properties were explored to understand the diffusion of Li^+ at atomic level. Radial distribution function (RDF) between Li^+ and Cl^- was observed to be strongly correlated and aggloromates upon increasing concentration of lithium salt. For the ethaline case, almost all the chloride ion i.e. ~ 100 was found to be involved in the hydrogen bonding as acceptor with the oxygen of ethylene glycol as donor, which significantly decreases upon increasing salt concentration unlike the case with glyceline. Therefore, chloride ions interacts strongly with the Li^+ of added salt resulting into agglomeration of Li–Cl particles. In addition,

*Corresponding authors
Email addresses: kishant@nitw.ac.in (Kishant Kumar), abharti@bitmesra.ac.in (Anand Bharti)

April 8, 2021

the diffusion coefficient decreases upon increasing salt concentration, which is possibly because of the agglomeration. Therefore, we propose the addition of Li–salt in an optimal and very low ratio to serve the purpose as an alternative to commercial electrolytes.

Keywords: Li-ion Battery, Electrolytes, Deep Eutectic Solvent, Molecular Dynamics Simulation

1. INTRODUCTION

Electrochemical reactions gained much attention in the field of energy storage and electrical energy devices. Among the wide variety of electrochemical cell, application and utilization of lithium ion batteries (LIBs) in the modern life is found to be most popular because of attractive high value of power to mass ratio, which is a breakthrough in the development of portable electronic gadgets. The electrochemical reactions at the electrode material and the migration of Li^+ ion are the two most important mechanism in the working of LIBs [1, 2, 3]. Extensive research are being carried out for the development of efficient electrodes for redox reactions. However, the transport properties of Li^+ ion also plays an important role in increasing the overall electrochemical performance. In this regard screening of suitable electrolyte could be done in such a way that it should possess low viscosity, high ionic conductivity, less toxic and easy to degrade by biological treatment [4, 5, 6, 7]. Solid electrolyte based on polyethylene oxide possess high electrochemical stability, easy fabrication, low cost and moreover safe to use at low to moderate temperature [8, 9, 10, 11]. However, solid electrolytes have low ionic conductivity due to high crystalline nature of the material[8]. Flammable and volatile liquids as an electrolyte in LIBs was believed to be the major concern, which led to the application of ionic liquids (ILs) as electrolytes. Non flammability and very low vapour pressure of ILs are observed to be better replacement of conventional electrolytes. Kono et al. reported the use of pure ionic liquid as an electrolyte for the first time and observed a stable and reversible capacity on graphitized negative electrode[12]. Kohl et

al. blended ILs with an appropriate percentage of organic solvent (propylene carbonate) as an electrolyte with silicon nanowire based anode, where it showed a good overall electrochemical performance [13]. In the past decade, an emerging solvent named deep eutectic solvents (DESs) attracted the attention because of its remarkable physicochemical properties compared to the organic solvents as well as ionic liquids[14]. It possesses good thermal and chemical stability, low volatility, and liquid under the region of low to moderate temperature[15, 16, 17]. In addition, DESs observed to be biodegradable, low toxicity, can be recycled, and cost effective product etc[17]. In spite of the fact that ILs and DESs share most of the desirable characteristics for electrolytes, later are easy to prepare at an effective low cost[18]. The emerging and potential application of DES is observed in metal extraction[19, 20, 21], liquid–liquid extraction[22, 23], gas solubility[24, 25], electrochemistry[15], and bioseparations[26]. In addition, DES could also emerge as an alternate electrolyte in LIBs. A best candidate for electrolytic application in lithium ion batteries can be characterised by its larger electrochemical window and high thermal and chemical stability, which is owned by the DESs[15]. Generally, DESs can be easily prepared by stirring the appropriate molar ratio of carboxylic acids and quaternary ammonium salts at a temperature of 100 C[14]. The liquid state of DES is achieved through depression in freezing point by hydrogen bonding between anion and a hydrogen bond donor (HBD). Therefore, the phase can be controlled by changing the molar ratio of anion and HBDs. Anouti et. al. used a DES prepared by compbination of N-methylacetamide and lithium bis[(trifluoromethyl)sulfonyl]imide as an electrolyte in LIBs and electric double later capacitors (EDLCs), which resulted to show good compatibility and excellent electrochemical performance with the activated carbon and LiFePO4 electrodes [27, 28]. Mustarelli et. al. explored two bio-inspired choline based DES viz. ethylene glycol (EG)/choline chloride (ChCl) and lactic acid/ChCl as an electrolyte added with lithium salt ($LiN(CF_3SO_2)_2$ and $LiPF_6$), in particular, the value of ionic conductivity at room temperature in the solution of 0.5 M $LiPF_6$/EG:ChCl was found to be 7.95 $mScm^{-1}$, which can serve as the green and low cost electrolyte[29].

In this work, the potential application of DESs as an alternative to commercially available electrolytes have been explored using the computational approach. For this purpose, molecular dynamics simulation was carried out for two DESs namely ethaline (1 ChCl + 2 Ethylene Glycol) and glyceline (1 ChCl + 2 Glycerol) in the presence of lithium based salt, Lithium Bis(trifluoromethanesulfonyl) imide ($LiTf_2N$). DES with varying concentration of $LiTf_2N$ (Li–salt) were studied to understand the structural and transport behaviour of Li^+ ion in DES at the molecular level.

2. COMPUTATIONAL DETAILS

2.1. OPLS Force field

Optimized potentials for liquid simulations for all–atom (OPLS–AA) was observed to accurately calculate the physical properties of several organic liquids[30]. Recently, Acevado et. al. revisited the OPLS–AA parameter for deep eutectic solvent (DES) to reproduce the accurate radial distribution function (RDF) and physical properties[31]. It was found that the slight scaling of partial charge and adjustment in bonded parameters reproduces the accurate fit of the energy minima from LMP2/cc-pVTZ(-f) calculations of the DES conformation[31, 32]. Thus, the OPLS–AA force field parameters modified by Acevado et. al. was used in this work to represent DESs. The added salt in the DES contains bis(trifluoromethylsulfonyl) imide ($[Tf_2N^-]$) anion and Li^+ as cation where the parameter of the combination of anion and cation were obtained from OPLS–AA and Aqvist's work respectively[33, 34]. The non-bonded potentials were described by the sum of electrostatic and Lennard-Jones (LJ) potentials, which was calculated using the equation 1. The bonded potential for intramolecular contribution was described by the sum of stretching, bending, dihedral torsion and improper terms given by the harmonic, harmonic, OPLS and OPLS functional form respectively, which was calculated using the equation 2. Intra and intermolecular interactions were not treated differently therefore 1–2 and 1–3 interactions were rounded off to zero while 1–4 interactions were scaled by 0.5

in order to use the same set of non-bonded potential parameters for both intra and intermolecular interactions. All the bonded and non-bonded potential parameters are depicted in the Table S1–S4 of supporting information while atom types are represented in the Figure 1.

$$\mathrm{U_{nb}} = \sum_{\mathrm{i>j}} \left[\frac{\mathrm{q_i q_j}}{4\pi\varepsilon_0 \mathrm{r_{ij}}} \right] + \sum_{\mathrm{i>j}} 4\epsilon_{\mathrm{ij}} \left[\left(\frac{\sigma_{\mathrm{ij}}}{\mathrm{r_{ij}}} \right)^{12} - \left(\frac{\sigma_{\mathrm{ij}}}{\mathrm{r_{ij}}} \right)^{6} \right] \tag{1}$$

$$\begin{aligned} \mathrm{U_b} = & \sum_{\mathrm{bonds}} \left[\frac{1}{2} \mathrm{k_b} (\mathrm{r} - \mathrm{r_e})^2 \right] \\ & + \sum_{angles} \left[\frac{1}{2} k_\theta (\theta - \theta_e)^2 \right] + \\ \sum_{dihedrals+improper} & \left[\frac{1}{2} \left[C_1(1 + cos(\Phi)) + C_2(1 - cos(2\Phi)) \right. \right. \\ & \left. \left. + C_3(1 + cos(3\Phi)) + C_4(1 - cos(4\Phi)) \right] \right. \end{aligned} \tag{2}$$

where U_{nb}, U_b are the non bonded and the bonded potential respectively. q_i and q_j are the partial charges on the i^{th} and j^{th} atoms respectively. r_{ij} is the distance between i^{th} and j^{th} atoms respectively. ϵ and σ are the well depths and Van der Waals radii respectively. k_b, k_θ and C's represents force constant for bond and angle as well as fourier constant respectively. r_e and θ_e defines the eqilibrium bond and angle values.

2.2. Molecular Dynamics Simulation

Two DESs namely ethaline and glyceline were studied at four different temperatures (298.15, 308.15, 318.15, 328.15 K) and at varying mole fraction of added salt ($\mathrm{LiTf_2N}$), which is summarized in Table 1. All the MD simulations were performed using the recent release version of GROMACS 2020.2 program[35]. First of all, 100 molecules of choline chloride (CC) and 200 molecules of hydrogen bond donors (HBDs) were packed in a cubic box of size 50 Å using the Packmol program[36]. A large cutoff of 16 Å was employed for LJ potential and short range electrostatic potential to minimize the error from the region of LJ tail and system size. The direct calculation of electrostatic

terms is computationally expensive therefore ewald summation techniques were performed using the particle-mesh ewald scheme (PME)[37]. The cross term LJ parameters were computed using the geometric mixing rule, which is given as $\sigma_{ij} = (\sigma_i \sigma_j)^{1/2}$ and $\epsilon_{ij} = (\epsilon_i \epsilon_j)^{1/2}$. Energy minimization of each system was carried out using the steepest-descent method until the maximum force converges to a value of 1000.0 kJ/mol/nm in order to remove any unfavourable contacts. Desired temperature during the MD simulation was achieved by rescaling the velocity of the atoms using a random factor, which is implemented in GROMACS as the term called v-rescale[38] while pressure was coupled in isotropic manner using Berendsen barostat[39]. The energy minimized structures were allowed to undergo annealing upto a temperature of 600K in order to obtain a lowest energy configuration at the desired temperature. A temperature versus time plot during the annealing is shown in the Figure S2 of supplementary information (SI). Annealing of the system was carried out in three cycles of heating and cooling within a time window of 0.3 nanosecond (ns) followed by the equilibration and production run in isothermal–isobaric (NPT) ensemble for a total time of 30 ns for RDF, coordination numbers (CNs) and H-bond analysis (structural properties). In addition, MD simulation of 70 ns were carried out with timestep of 1 femtosecond in Canonical (NVT) ensemble for the accurate calculation of self-diffusion coefficients. It is also important to note that the system size of DES (100 ChCl/200 Etg) were found to be accurately mimic the bulk density of the DES among the three different system size of 100, 150 and 200 DES as shown in the Figure S1 of SI.

3. RESULTS AND DISCUSSION

3.1. Density

Figure 2 and Table 2 shows the comparison between computed density and experimental density of pure ethaline and glyceline at different temperature. A good agreement was found between simulated and experiment density with an error of less than 2%. Figure 2 also summarizes the density of Li–salt +

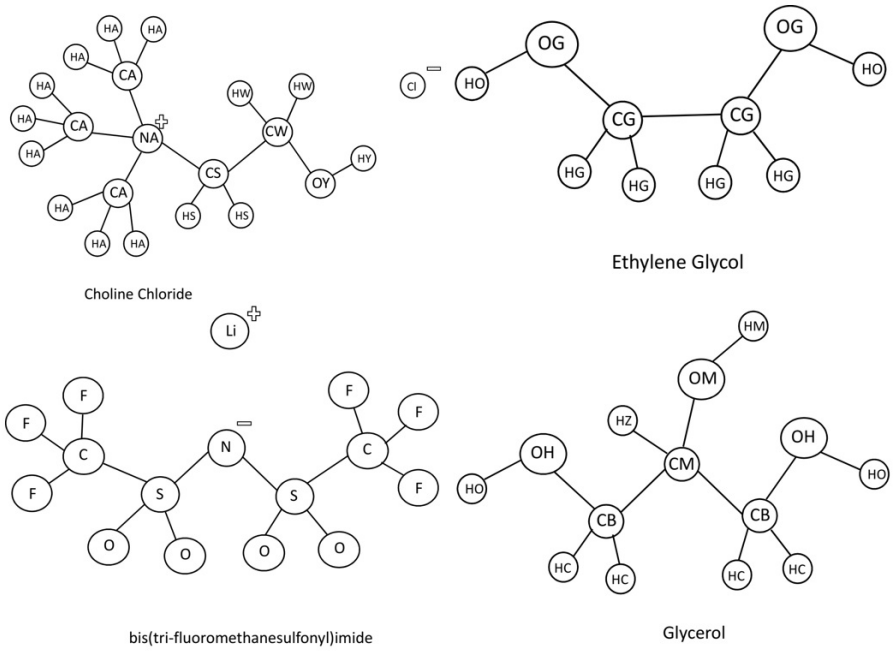

Figure 1: Description of anions/cations and neutral molecule based on atom-type used in this work

Table 1: Various electrolyte prepared by addition of Li–salt in different mole fraction into DES (CC and HBDs).

Abbreviation	**HBDs**	**mole fraction $LiTf_2N$**
CCEtg (Ethaline)	Ethylene Glycol (Etg)	0.00
CCEtg+0.05mf	Ethylene Glycol (Etg)	0.05
CCEtg+0.1mf	Ethylene Glycol (Etg)	0.10
CCEtg+0.2mf	Ethylene Glycol (Etg)	0.20
CCEtg+0.3mf	Ethylene Glycol (Etg)	0.30
CCEtg+0.5mf	Ethylene Glycol (Etg)	0.50
CCGly (Glyceline)	Glycerol(Gly)	0.00
CCGly+0.05mf	Glycerol(Gly)	0.05
CCGly+0.08mf	Glycerol(Gly)	0.08
CCGly+0.2mf	Glycerol(Gly)	0.20
CCGly+0.3mf	Glycerol(Gly)	0.30

Table 2: Calculated density (kg/m^3) for pure DES and Li–salt solution (density averaged over last 15 ns out of 30 ns trajectory from NPT ensemble)

Composition	**Temperature (K)**			
	298.15	**308.15**	**318.15**	**328.15**
CCEtg (Ethaline)	1109.64	1101.29	1094.52	1086.62
CCEtg+0.05mf	1135.89	1127.32	1117.84	1110.48
CCEtg+0.1mf	1161.91	1153.91	1144.57	1136.8
CCEtg+0.2mf	1219.56	1209.48	1202.16	1192.14
CCEtg+0.3mf	1281.99	1273.8	1263.31	1253.2
CCEtg+0.5mf	1425.22	1415.1	1401.92	1390.72
CCGly (Glyceline)	1191.27	1187.64	1182.52	1176.35
CCGly+0.05mf	1213.24	1207.78	1202.6	1195.33
CCGly+0.08mf	1230.01	1224.99	1217.42	1209.97
CCGly+0.2mf	1287.09	1282.5	1273	1266.55
CCGly+0.3mf	1342.33	1334.45	1326.61	1320.12

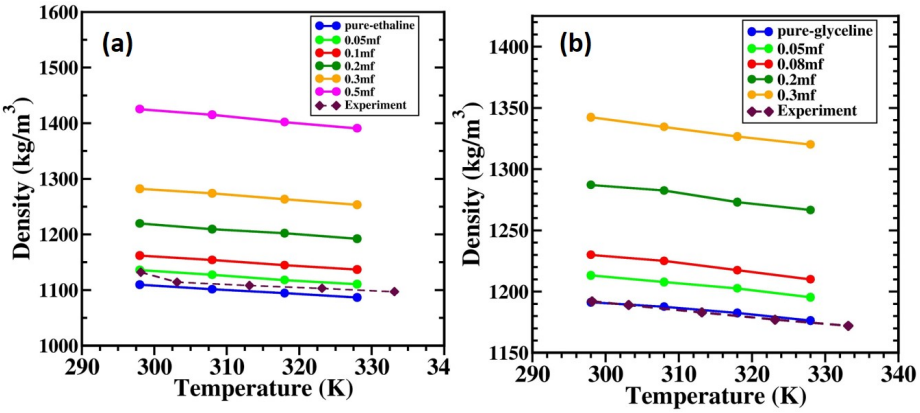

Figure 2: Density of (a) Ethaline + $LiTf_2N$ (b) Glyceline + $LiTf_2N$. Note: Experimental density data[31] in the both cases are shown by dotted line (cyan colour with diamond symbol)

DES system at 1 atm as a function of temperature (298.15, 308.15, 318.15 and 328.15 K) and mole fraction of Li–salt in DES. It can be observed from the Figure 2 that the solution density is found to be more dependent on the mole fraction at a particular temperature. It can also be seen from Figure 2 (a) & (b) that the solution density increases as the mole fraction increases at a particular temperature. The general trend for the solution density was observed for all the solution studied in this work. When high amount of Li–salt was added in DES, the solution density was found to increase significantly due to agglomeration of Li–salt.

3.2. Radial Distribution Function (RDF) and Coordination Number (CN)

In order to understand the structural arrangement of Li–salt around DES, radial distribution function (RDF) and corresponding cumulative CN were computed upto the first solvation shell using equation 3 and 4 respectively.

$$g_{i,j}(r) = \frac{n(r)}{4\pi r^2 dr \rho} \tag{3}$$

$$N_{i,j}(R) = \int_0^R g_{i,j}(r) dr \tag{4}$$

Where computation of RDF in equation 3 includes the term r and dr as shell distance from the reference atom i and thickness of the shell at distance r respectively. n(r) is the number of atom j within the distance of r from the reference atom i, while $4\pi r^2 dr$ represents volume of the concentric shell of thickness dr. ρ is the number bulk density of j atoms. During the calculation of CN, $N_{i,j}$ is the number of j atoms within the sphere of radius R from the i^{th} atom (as reference atom).

The centre of mass was considered for $Chol^+$, Etg, Gly and Tf_2N^- while computing the RDF and CN between the different fragments. The last 5 ns trajectory was used for RDF calculation, which was averaged over 5000 frames during 5 ns.

3.2.1. RDF of ethaline system

Figure 3 (a) & (e) depicts the arrangement of Cl^- ion around centre of mass of Etg and $Chol^+$ cation, respectively. The first peak was found at 4.32 Å for Etg–Cl^- and 4.11 Å for $Chol^+$–Cl^-. CN was also computed for the first solvation shell by evaluating the integral of g(r) averaged over the distance. The first solvation shell was defined as the region within the first minimum of the function g(r). A distance of 5.6 Å and 4.6 Å was found to be the region of first solvation shell for Etg–Cl^- and $Chol^+$–Cl^- respectively (Figure 6 (a)). CN was observed to be in the range of 1–1.5 for both and remains unaffected by mole fraction of Li–salt. Figure 3 (c) & (d) shows the RDF between Etg–Etg and $Chol^+$–$Chol^+$ respectively, where the first wide peak was obtained at 4.86 Å and 6.6 Å respectively and was unaffected by the addition of Li–salt. CN of Etg around Etg and $Chol^+$ around $Chol^+$ are shown in the Figure 6 (a), where CN was found to be in the range of 5.1–4 and 5.1–3 respectively, which decreases with increasing salt concentration. A wide peak was obtained at 5.41 Å for Etg–$Chol^+$, where intensity of the peak remains unaffected by salt concentration upto 0.3mf followed by a reduced intensity for the 0.5mf salt solution. CN for the Etg–$Chol^+$ slightly decreases with increasing salt concentration upto 0.3mf as shown in Figure 6 (a) followed by a significant decrease in CN for 0.5mf, which

inferred that the structural order of ethaline does not prevails for higher salt concentration. Figure 3 (f) shows the RDF for Cl^-–Cl^-, where an increased intensity peak was observed to be salt concentration dependent, highest for 0.5mf at 3.74 Å. The number of Cl^- around Cl^- appeared in the range of 0–4, which increases with increase in salt concentration within the first solvation shell of 4.3 Å (Figure 6 (a)).

Tf_2N^-–$Chol^+$ and Tf_2N^-–Etg showed the first wide peak at 5.71 Å and 5.35 Å respectively (Figure 4 (a) & (b)). CN increases with increase in salt concentration for both $Chol^+$–Tf_2N^- and Etg–Tf_2N^-, (Figure 6 (b)) but it is clearly visible that the interaction of Etg (i.e HBD) with Tf_2N^- (i.e salt anion) is dominant than the interaction between $Chol^+$ and Tf_2N^-. In order to quantify the comparative interaction strength for HO–Cl and HY–Cl , RDF was calculated for both the cases. The first intense peak was observed at 2.11 and 2.37 Å for HO–Cl and HY–Cl respectively (Figure 4 (c) & (e)). But the intensity of the peak for HO–Cl was almost twice higher that of HY–Cl , which indicates strong interaction between HO of Etg and Cl^- (note that the first intense peak in RDF correspond to the electrostatic interaction). Nevertheless, the interaction between $Chol^+$ and Cl^- as well as Etg and Cl^- plays a significant role in the formation of deep eutectic solvent owing to its very close contact of less than 3 Å, which is the limit of a strong hydrogen bonding. It should also be noted that the intensity of peak decreases as the salt concentration increases. In addition, possibility of intermolecular hydrogen bonding between $Chol^+$ (atom type OH) and Etg (atom type OG) as well as Etg (atom type OG) and Etg (atom type OG) were explored using RDF study. It is evident from Figure 4 (d) & (f), that the first peak was observed at 1.88 and 2.00 Å, which is due to the strong electrostatic interaction responsible for the formation of intermolecular hydrogen bonding. The hydrogen bonding between HO and OG i.e. between the two Etg was stronger than the hydrogen bonding between $Chol^+$ and Etg, which can be confirmed by the intense and nearer peak observed in Figure 4 (d).

Li^+ and Cl^- possess a strong positive and negative partial charge, respec-

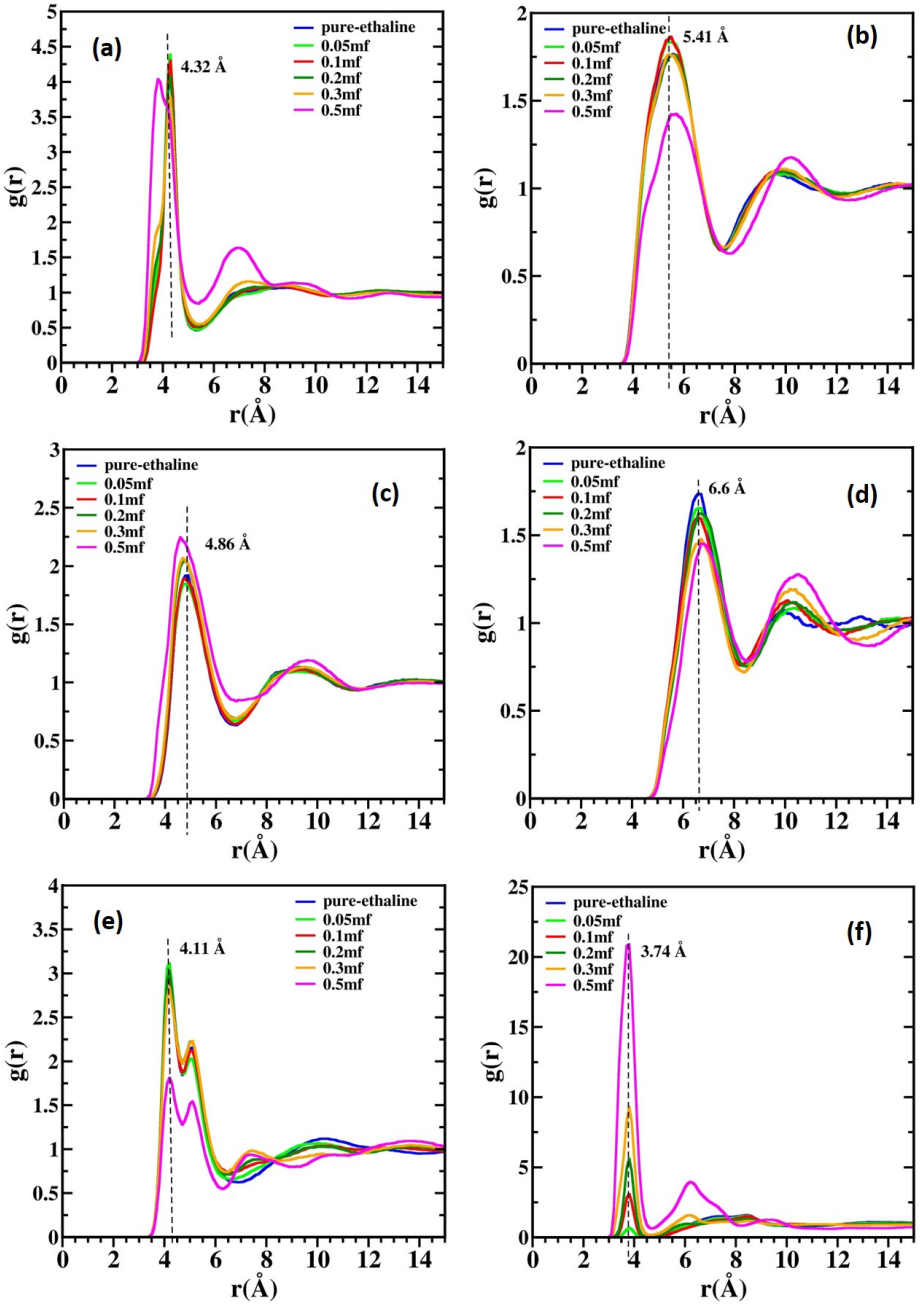

Figure 3: RDFs of (a) Etg–Cl^-, (b) $Chol^+$–Etg, (c) Etg–Etg, (d) $Chol^+$–$Chol^+$, (e) $Chol^+$–Cl^-, and (f) Cl^- Cl^- in ethaline solution as a function of the mole fraction of Li–salt at 298.15 K

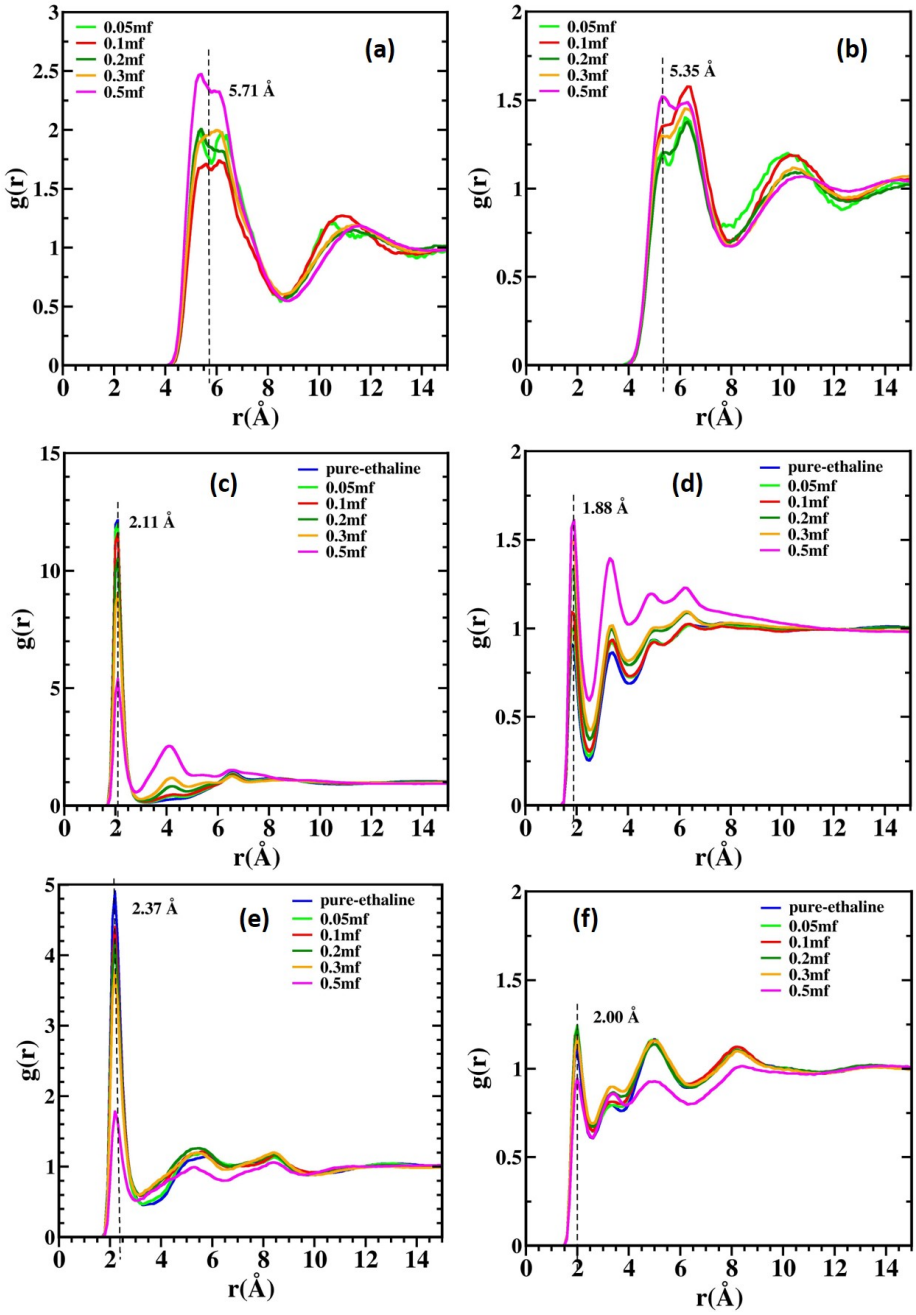

Figure 4: RDFs of (a) $Chol^{+}$–Tf_2N^{-}, (b) Etg–Tf_2N^{-}, (c) HO–Cl^{-}, (d) HO–OG, (e) HY–Cl^{-}, and (f) HY–OG in ethaline solution as a function of the mole fraction of $LiTf_2N$ salt at 298.15 K

tively. RDF was calculated for Cl^- around Li^+ and an intense peak at 2.21 Å was found (Figure 5 (a)). This peak is attributed to the strong electrostatic interaction while the second peak increases with the increase in salt concentration because of increased van der Waals interaction. CN first increases from 2.0 to 3.0 and then decreases upto 2.25 on increasing salt concentration (Figure 6 (b)). Similarly, the interaction between the hydroxyl group of Etg and Li^+ was understood through RDF, which appears to be significantly concentration dependent as shown in the Figure 5 (b). In addition, from the Figure 5 (d), the possibility of hydrogen bonding between $Chol^+$ and Etg was confirmed by an intense peak at 2.0 Å only at salt concentration of 0.5mf while at other less composition, a less intense peak was observed at 1.88 Å. The structural order of Tf_2N^- around Tf_2N^- was improved at concentration other than 0.05mf (Figure 5 (c)), confirming the solution has an improved and ordered structure.

3.2.2. RDF of glyceline system

The first intense peak for Cl^-–Gly and Cl^-–$Chol^+$ was observed at 4.76 and 4.11 Å respectively (Figure 7 (a) & (e)). An almost constant CN of 1.5 was seen for both the cases irrespective of salt concentration (Figure 10 (a)). RDF between Gly–Gly and $Chol^+$–$Chol^+$ was analysed and first wide peak was seen at 5.43 and 6.28 Å respectively (Figure 7 (c) & (d)) for all salt concentration. The number of Gly around Gly and $Chol^+$ around $Chol^+$ was evaluated to be 7.5 and 5.0 respectively in the case of pure glyceline, while a decreasing CN was observed with increasing salt concentration as depicted in the Figure 10 (a). A wide peak at 5.86 Å was confirmed through Figure 7 (b) for Gly around $Chol^+$ where 8 nos. of Gly molecules were present around $Chol^+$ within the first solvation shell of 7.6 Å, which is further found to be decreasing upon increasing salt concentration as shown in the Figure 10 (a). In addition, a very wide and less intense peak was observed for Cl^- around Cl^- at 6.74 Å in pure glyceline system, while at increased salt concentration, the peak shifted to 4 Å followed by an increased intensity of peak from 0.05mf to 0.3mf (Figure 7 (f)). The first solvation shell for the added lithium salt was observed at 4.5 Å, where CN was

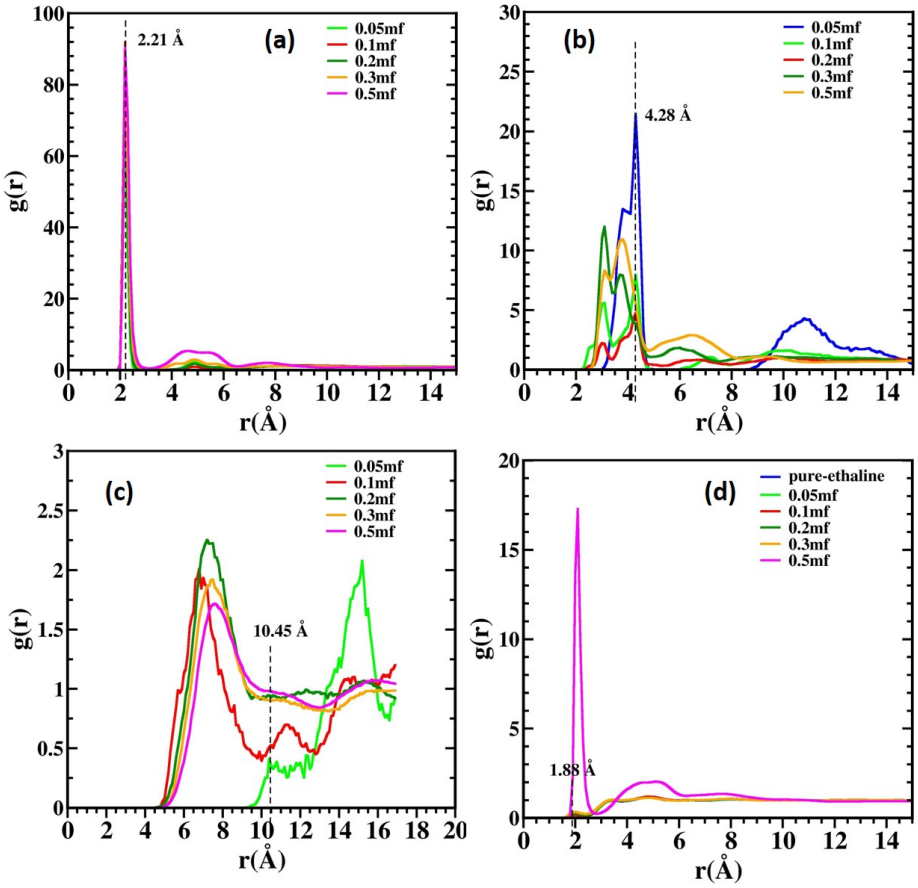

Figure 5: RDFs of (a) Li^+–Cl^-, (b) Li^+–OG, (c) Tf_2N^-–Tf_2N^-, (d) OY–HO in ethaline solution as a function of the mole fraction of $LiTf_2N$ salt at 298.15 K

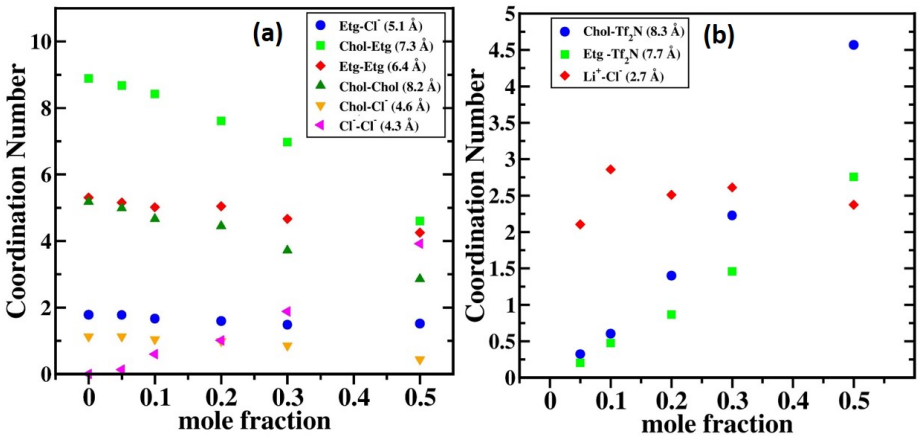

Figure 6: CNs of different species in Ethaline + Li–salt system at varying mole fraction of Li–salt. a) CN between different components within Ethaline b) CN between the components of Ethaline and Li–salt. Note that the CN calculated within the distance of first solvation between different species (centre of mass), distance shown in the legend is the first solvation distance just before the first minima in RDF peak.

seen to increase with an increased salt concentration as shown in Figure 10 (a).

Likewise, ethaline, structural arrangement of Tf_2N^- ions around $Chol^+$ and Gly were analysed with the help of RDF calculations. Figure 8 (a) & (b) confirms the presence of Tf_2N^- around $Chol^+$ and Gly at the minimum distance of 6.32 and 5.41 Å, respectively. In addition, Figure 10 (b) shows CN value of Tf_2N^- around the $Chol^+$ and Gly, which is found to be increasing with increase in salt concentration, possibly because of the favourable interaction between the species. Hydrogen bonding was also confirmed through RDF plot as shown in Figure 8 (c), (e) & (f). Figure 8 (e) shows the first intense peak at round 2.27 Å, which also justify the presence of hydrogen bond among donor and acceptor group in glycerol (HBD) molecule. Chloride ion being highly negative charge possess the capability to interact with the atom types having strong partial positive charge such as HO and HY, which can be clearly seen from the first intense peak at 2.18 and 2.15 Å as shown in the Figure 8 (c) & (f) respectively. In addition, a possible strong interaction between Cl^- and HM was explored, which can be justified from the first intense peak at 2.33 Å (Figure 8 (d)).

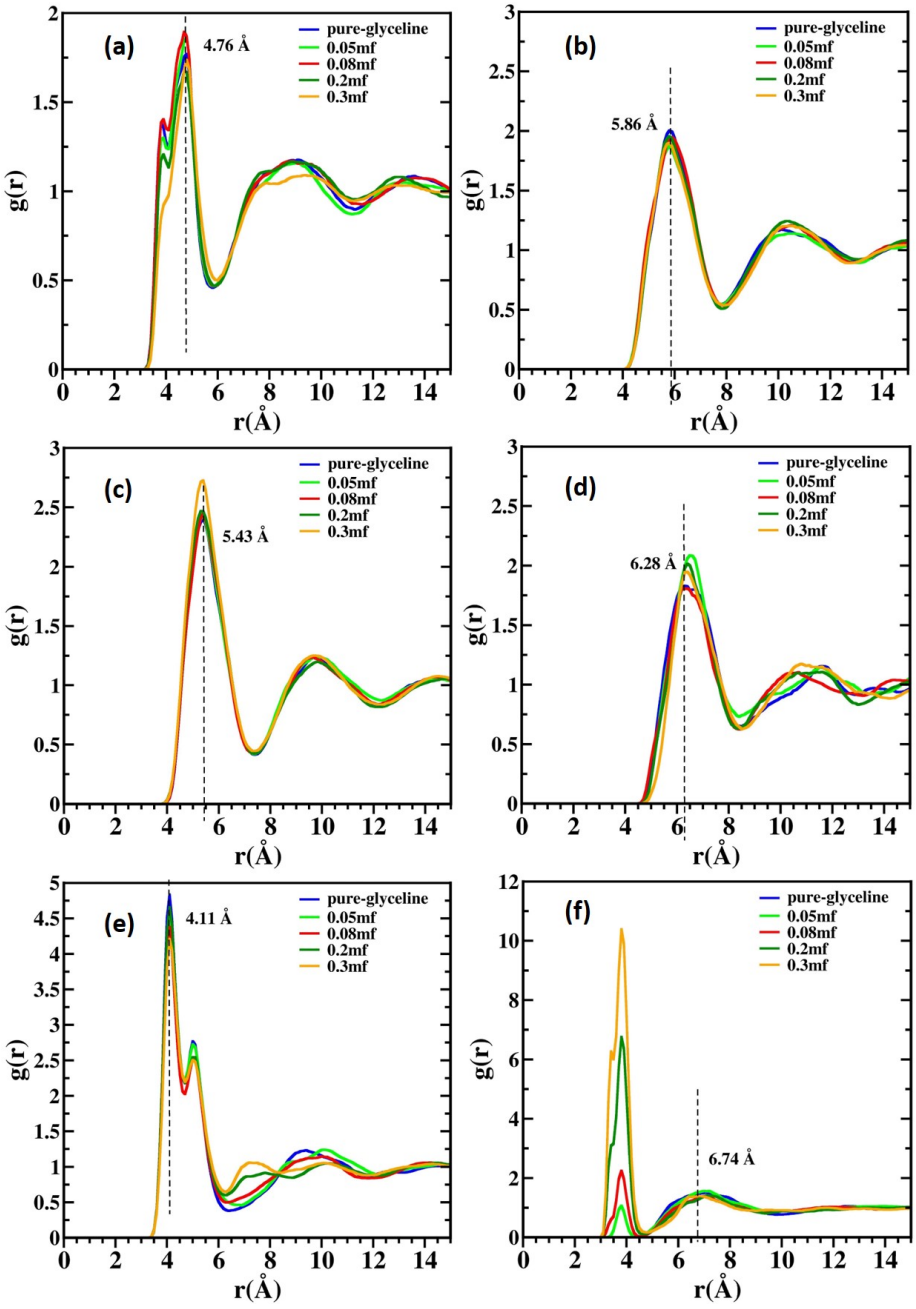

Figure 7: RDFs of (a) Gly–Cl^-, (b) Gly–$Chol^+$, (c) Gly–Gly, (d) $Chol^+$–$Chol^+$, (e) Cl^-–$Chol^+$, and (f) Cl^-–Cl^- in glyceline solution as a function of the mole fraction of $LiTf_2N$ salt at 298.15 K

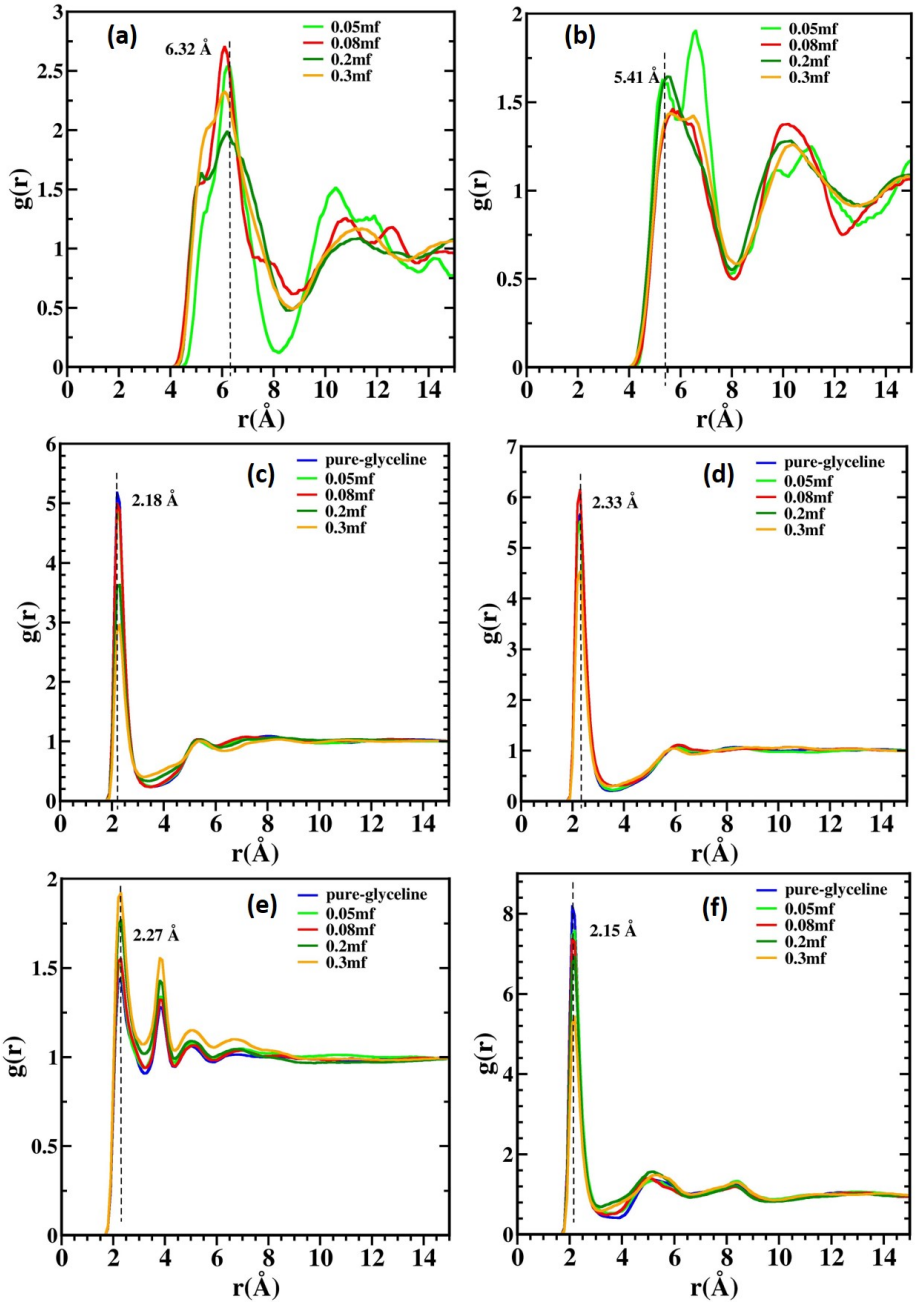

Figure 8: RDFs of (a) $Chol^{+}$–Tf_2N^{-}, (b) Gly–Tf_2N^{-}, (c) HO–Cl^{-}, (d) HM–Cl^{-}, (e) HO–OH, and (f) HY–Cl^{-} in glyceline solution as a function of mole fraction of $LiTf_2N$ salt at 298.15K

Presence of Li^+ and Cl^- in the electrolyte salt solution plays an important role in charge diffusion because of their smaller size than other species. Lithium being positive while chloride possess negative charge tends to form a strong interaction, which was confirmed by the first intense peak at 2.21 Å (Figure 9 (a)). The effect of increasing salt concentration was seen to have an increasing CN value on addition of salt from 0.05mf to 0.08mf. Further increase in concentration have insignificant effect on CN values and remains almost constant. Structural Correlation between Tf_2N^- and Tf_2N^- is depicted in Figure 9 (c), where the first broad peak was observed at 6.32 Å for 0.05mf solution, followed by the reduced intense peak for other salt concentration. Li^+ shows an interacting behaviour with glycerol (HBD), Figure 9 (d) shows an intense peak at 2.18 Å, probably because of the strong electrostatic interaction between partial opposite charges.

3.3. Hydrogen Bond Analysis

The possibility of hydrogen bond was explored through geometry based H–Bond analysis. Several hydrogen bonds were identified in Li–salt + DES electrolyte system, which is shown in SI as a schematic diagram (Figure S4). Two criterion was used for the quantification of hydrogen bond between the different atom types in the system: cut-off distance of 3.0 Å and an angle of 30°, which was done using H-bond plugin implemented in VMD[40]. The average number of H–bond reported in this work was calculated over last 5 ns of trajectory collected after every 1 picosecond i.e 5000 configurations.

3.3.1. Ethaline–Tf_2N^- salt

Four different types of hydrogen bond were observed in the ethaline based electrolyte viz. (i) between Cl^- and Etg i.e Cl^-(acceptor)—OG(donor) (ii) between Etg and Etg i.e OG —OG (both as donor and acceptor) (iii) between $Chol^+$ and Etg i.e OY—OG (both donor and acceptor) (iv) between Cl^- and $Chol^+$ cation i.e Cl^- (acceptor)—OY (donor). From Figure 11 (a), it is confirmed that the approximately 100 number of H–bond formed between Cl^- and

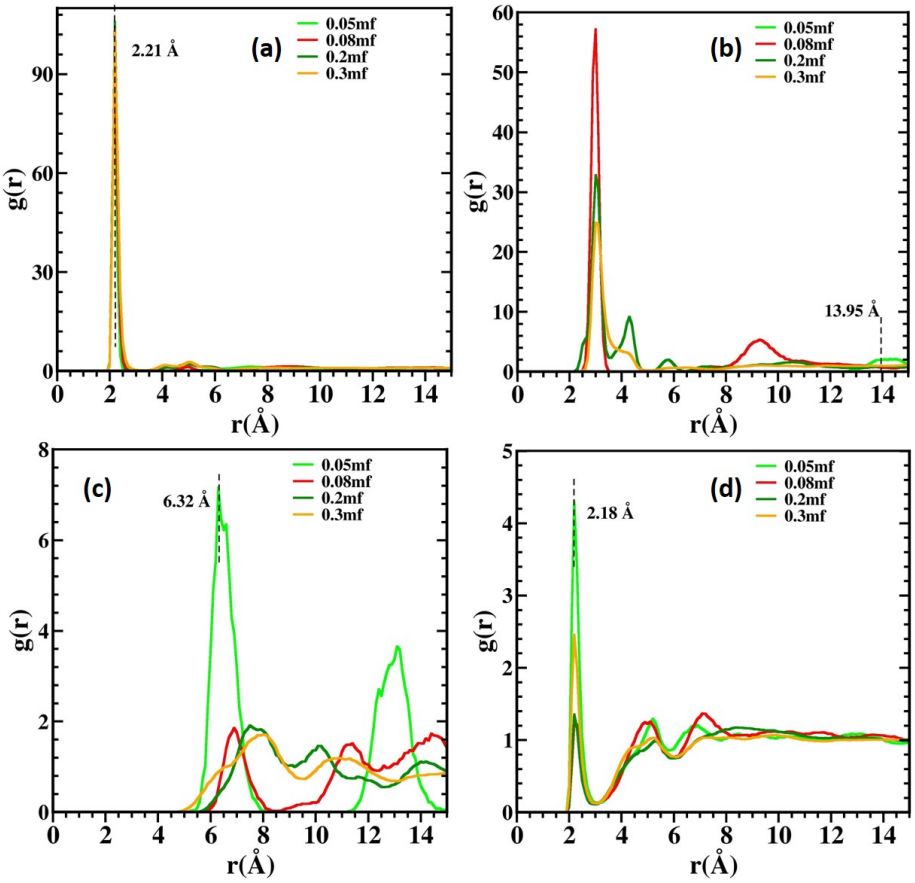

Figure 9: RDFs of (a) Li^+–Cl^-, (b) Li^+–Li^+, (c) Tf_2N^-–Tf_2N^-, (d) Li^+–OH in glyceline solution as a function of the mole fraction of $LiTf_2N$ salt at 298.15 K

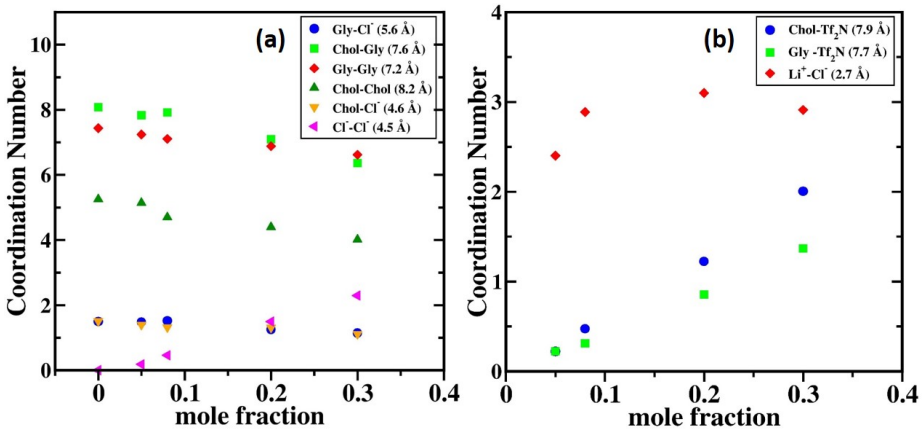

Figure 10: CNs of different species in Glyceline + Li–salt system at varying mole fraction of lithium salt. a) CN between the different components within Glyceline b) CN between the components of Glyceline and Li–salt. Note that the CNs calculated within the distance of first solvation between different species (centre of mass), distance shown in the legend is the first solvation distance just before the first minima in RDF peak.

hydroxyl group of Etg (OG as donor), which was found to be decreasing significantly upon increasing the salt concentration (blue solid circle of Figure 11 a), possibly due to increased interaction between the added salt species and DES. Interestingly, upon addition of salt concentration, H–bond between two hydroxyl groups of the Etg first increased and then decreased at high salt concentration (green solid square of Figure 11 a), possibly due to decreased number of H–bond between Cl^- and hydrogen atom connected to OG of Etg resulting to an increase in H–bond between two hydroxyl group. In addition, at a high mole fraction of 0.5mf, the number of H–bond was found to decrease possibly due to phase transition upon addition of significant amount of salt. The H–bond between hydroxyl group in $Chol^+$ cation and Etg was analysed, where OY of $Chol^+$ cation and OG of Etg was found to act as a donor as well as an acceptor (red solid diamond symbol of Figure 11 b), which decreases upon increasing salt concentration, probably due to increased interaction between the added salt and the species involved in the formation of DES. It was also observed that the Cl^- ion (as acceptor) forms H–Bond with the hydrogen atom connected to OY

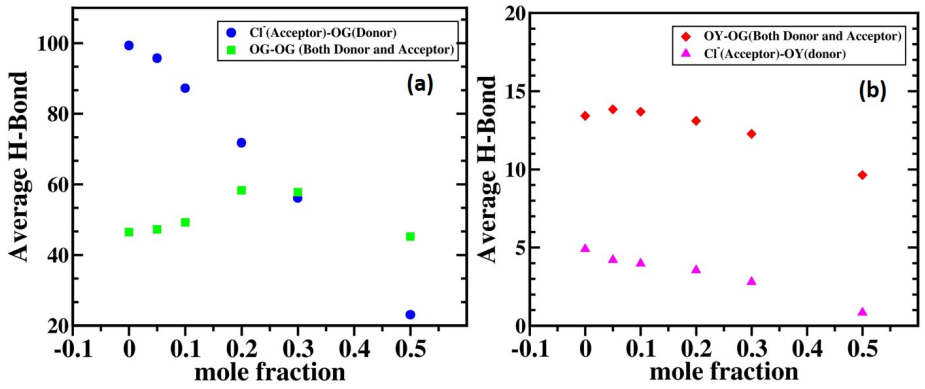

Figure 11: Average number of H–Bond shown for ethaline system in varying salt concentration. Definition of donor/acceptor and atom types are shown in the SI of Figure S3 and Figure 1 respectively a) blue solid circle represents the H–Bond between Cl^- ion and hydrogen atom bonded with donor atom OG in Etg (HBD), while green solid square shows the H–bond between OG and hydrogen atom bonded to OG in Etg (where OG can act as donor as well as acceptor both) b) red solid diamond symbol represents the H–Bond between the first group OY–HY of $Chol^+$ and second group OG–HO in Etg while pink solid triangle symbol shows the H–bond between Cl^- ion and HY bonded to OY (donor) in Etg.

as donor atom in Etg (pink solid triangle symbol of Figure 11 b), which was found to be in a very insignificant amount, confirming the presence of strong interaction between Cl^- and OG.

3.3.2. Glyceline–Tf_2N^- salt

In the glyceline based electrolyte, four possible hydrogen bonds were identified as, i) between Cl^- and glyceline i.e Cl^- (acceptor)—OH (donor) ii) between glycerol and glycerol i.e OH—OH (both as donor and acceptor) iii) between $Chol^+$ and glycerol i.e OY—OH (both as donor and acceptor) iv) between Cl^- (as acceptor) and $Chol^+$ (as donor). Number of H–bond between glycerol and glycerol (OH and OH respectively both as donor and acceptor) was seen to be unchanged by varying the salt concentration (Figure 12 green solid square symbol). Similarly, the number of H–bond between $Chol^+$ and glycerol (OY and OH respectively both as donor and acceptor) was also seen to be independent of salt concentration (red solid diamond symbol in Figure 12). The average num-

ber of H–bond between Cl^- and hydrogen atom bonded to OH atom type in glycerol was found to be almost unchanged upto a salt concentration of 0.08mf (blue solid circle symbol in Figure 12), while it further decreases with increase in salt concentration possibly because of increased interaction of Cl^- with Li^+ as shown in Figure 14. Similarly, it can also be explained from Figure 14, that the number of average H–bond between Cl^- and hydrogen atom attached to OY of $Chol^+$ decreases with increased salt concentration.

3.4. Diffusivity Calculation

Self-diffusion coefficient was calculated for the lithium and chloride ions to quantify the mobility in the DES based electrolytes. Self-diffusion coefficient can be computed using the Einstein's relation, which is given by the equation 5.

$$\mathrm{D_{self}} = \frac{1}{6} \lim_{\mathrm{t'}\to\infty} \frac{\mathrm{d}}{\mathrm{dx}} \left\langle \sum_{\mathrm{i=1}}^{\mathrm{N}} [\overrightarrow{r_i}(\mathrm{t}+\mathrm{t'}) - \overrightarrow{r_i}(\mathrm{t})]^2 \right\rangle \tag{5}$$

$$\beta(\mathrm{t}) = \frac{\mathrm{d}\log_{10}\left\langle \left(\Delta \mathrm{r(t)}^2\right)\right\rangle}{\mathrm{d}\log_{10}\mathrm{t}} \tag{6}$$

where, N represents number of total particles to be considered, $\overrightarrow{r}$ is the position vector of the particle, while t and t' are the time and change in time respectively.

Diffusion coefficient was computed at low temperature range of 298K – 328 K after extrapolating the data obtained in the range of 400 K – 490 K on linear scale. The fitted parameter and diffusivity at low temperature is provided in the Table S7 – S10 in the SI. Addition of lithium salt ($LiTf_2N$) into the liquid DES results into the formation of complex phase, where it was difficult to obtain a diffusive regime for the Li^+ ion to apply the Einstein's relation. Therefore, beta parameter was first evaluated to locate the trajectory in the diffusive regime, a value near to one shows the diffusive regime. First of all, the time region was found in which the was observed to be almost one using the equation 6 and the self-diffusion coefficient was computed in that time interval using

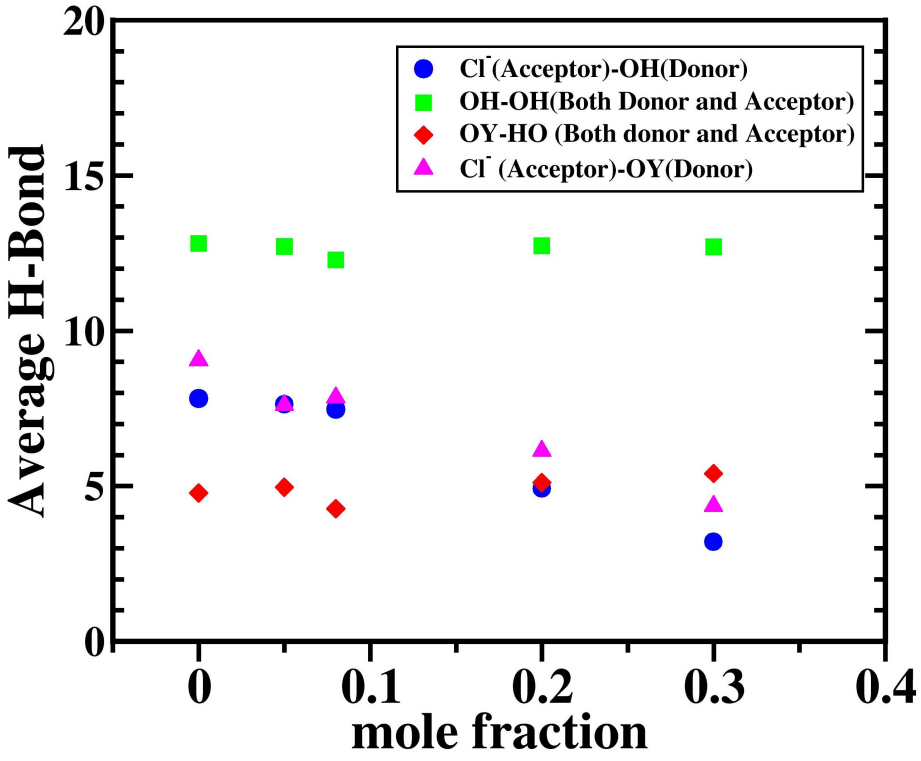

Figure 12: Average number of H–Bond shown for glyceline system for varying salt concentration. a) blue solid circle shows the H–Bond between Cl^- ion and hydrogen bonded with donor atom OH in Gly (HBD), green solid square shows the H–bond between OH and hydrogen atom bonded to OH in Gly (where OH can act as donor as well as acceptor both), red solid diamond symbol represents the H–Bond between the first group OY–HY of $Chol^+$ and second group OH–HO in Gly and pink solid triangle symbol shows the H–bond between Cl^- ion and HY bonded to OY (donor) in Gly

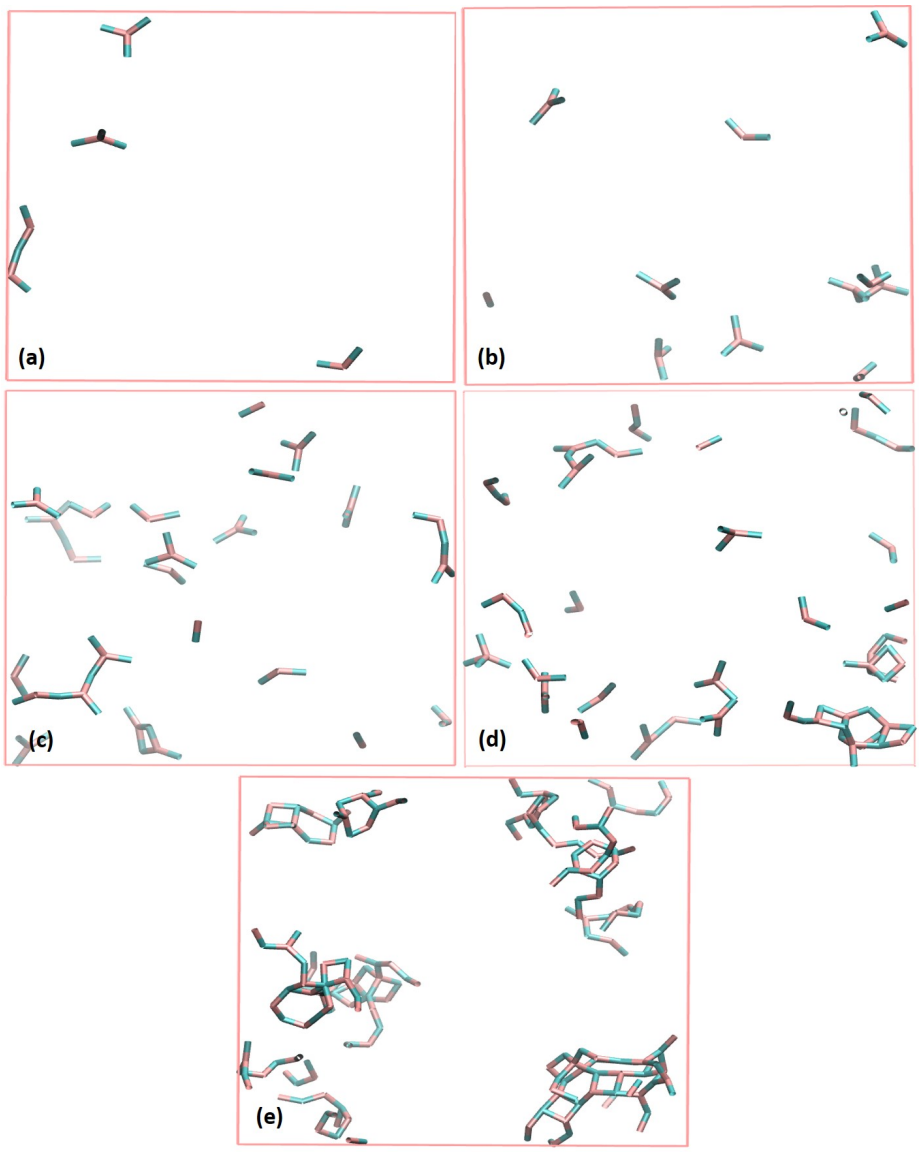

Figure 13: Snapshot for the arrangements of Li^+ and Cl^- ions in Ethaline system, stick model representing the nearest Cl^- contact (grey as Cl^- side) around the Li^+ ion (pink as Li^+ side) within a distance cut-off of 2.5 Å. a) 0.05mf b) 0.1mf c) 0.2mf d) 0.3mf and e) 0.5mf Note: All atoms other than the close contact between Li^+ and Cl^- were omitted for clarity.

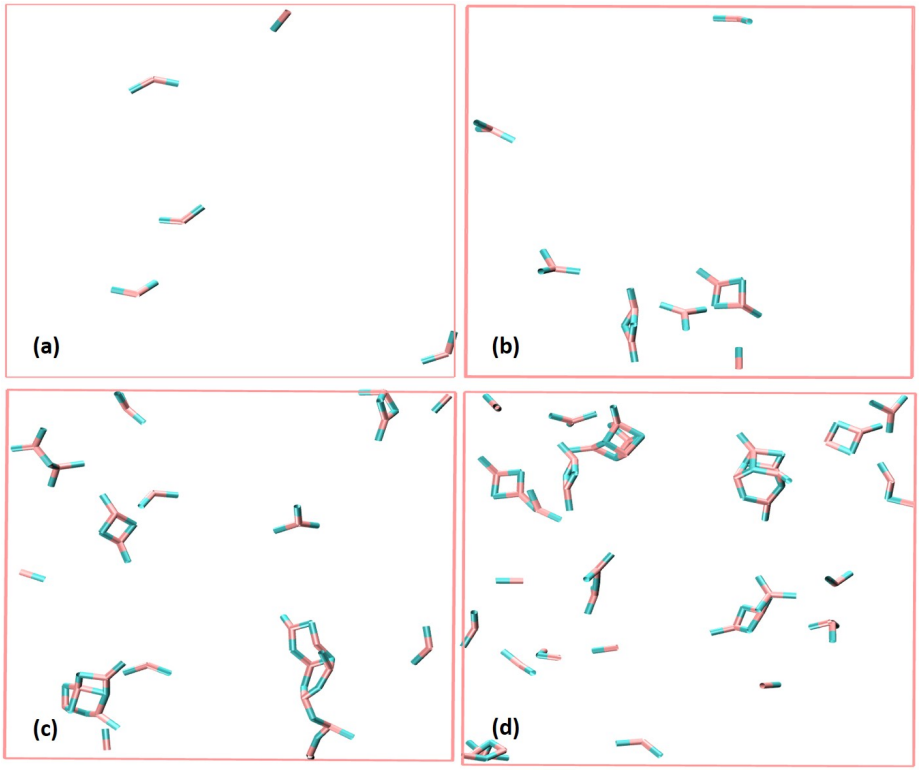

Figure 14: Snapshot for the arrangements of Li^+ and Cl^- ions in Glyceline system, stick representing the nearest Cl^- contact (grey as Cl^- side) around the Li^+ ion (pink as Li^+ side) within a distance cut-off of 2.5 Å. a) 0.05mf b) 0.08mf c) 0.2mf d) 0.3mf Note: All atoms other than the close contact between Li^+ and Cl^- were omitted for clarity.

Table 3: Self-diffusion coefficient (10^{-11} m^2s^{-1}) of Li^+ and Cl^- between the temperature and concentration (Tf_2N^-) range of 400–490 K and 0.0–0.2mf respectively in the ethaline based electrolytes.

	Cl^-				**Li^+**		
T (K)	**Pure Ethaline**	**0.05mf**	**0.1mf**	**0.2mf**	**0.05mf**	**0.1mf**	**0.2mf**
400	43.51	36.36	35.82	28.52	17.17	23.40	14.60
430	75.36	75.08	68.20	50.29	31.19	35.58	34.02
460	111.1	111.1	95.35	82.87	48.29	51.45	45.09
490	157.8	155.3	143.2	108.3	102.2	84.88	79.68

the equation 5. It can be visualized from the Figure 13 & 14 that the Li^+ strongly interacts with Cl^- and hence mobility of Li^+ ion significantly depends on the concentration of added lithium salt in the DES. For the case of ethaline (Table 3), self-diffusion coefficient of Cl^- and Li^+ increases with increase in temperature while the self-diffusion coefficient of Cl^- decreases on increasing salt concentration in DES, possibly because of the increased interaction with Li^+ in the electrolyte system. It can be observed from the dynamics of MD simulation (Figure 13 & 14) that one Li^+ is stabilized by maximum three Cl^- and upon further addition of Li–salt results into an increase in Li^+ diffusion followed by a decrease in diffusion at higher salt concentration (see Table 3). For the glyceline system, the temperature dependence of the diffusion coefficient was calculated where higher temperature shows an increasing diffusion coefficient. Dependence of Cl^- and Li^+ diffusion coefficient in the increasing lithium salt concentration was explored in this study, where the diffusivity of Cl^- and Li^+ decreases with increasing salt concentration, possibly because of the cluster formation between Li^+ and Cl^- ions due to large electrostatic interaction (Table 4).

Table 4: Self-diffusion coefficient (10^{-11} m^2s^{-1}) of Li^+ and Cl^- between the temperature and concentration (Tf_2N^-) range of 400–490 K and 0.0–0.2mf respectively in the glyceline based electrolytes.

	Cl^-				**Li^+**		
T (K)	**Pure Glyceline**	**0.05mf**	**0.08mf**	**0.2mf**	**0.05mf**	**0.08mf**	**0.2mf**
400	7.428	7.322	6.989	4.525	2.471	2.233	2.108
430	18.79	16.87	14.87	9.682	5.904	5.360	3.619
460	33.03	27.21	28.08	15.94	10.86	9.254	7.888
490	57.42	48.18	41.85	26.56	16.99	14.83	10.92

4. CONCLUSION

In the present work, the MD simulation was performed to investigate the structural and transport properties of lithium ions in the DES based electrolytes using RDF, CN, hydrogen bonding analysis and diffusivity calculations. Density obtained from MD simulation showed a good agreement with the experiment, which justified the applicability of the force field. Further, RDF between the different chemical species were computed in order to understand the structural correlations between the species. A strong intensity of g(r) was observed for the Cl^-/Cl^- and Li^+/Cl^- in the ethaline as well as glyceline system because of a strong electrostatic interaction between the positively and negatively charged ions, which was later confirmed by the visualization of only Li^+ and Cl^-. Several OH group in choline as well as in HBDs also played an important role in stabilizing the DES, which was further maintained even after addition of lithium salt. CNs within the first solvation distance showed a quantitative idea regarding the spatial distribution of chemical species. In addition, possibility of hydrogen bonding was also explored, which decreases upon increasing salt concentration or remains constant for few cases, except the hydrogen bonding

between OG—OG, which increases and then decreases upon increasing salt concentration. A cluster formation was observed between Li^+ and Cl^- ions upon increasing the salt concentration, followed by decrease in ion diffusivity. Therefore, a low and optimized concentration of lithium salt could be the best way for the preparation of electrolytes in battery application.

ACKNOWLEDGEMENTS

We wish to acknowledge the department of chemical engineering at National Institute of Technology Warangal, Telangana, India (NITW) for providing access to design and simulation laboratory for carrying out research work related to computer simulation. We thank Dr. Imre Bako at Research Centre for Natural Sciences, Hungary and Dr. Rajasekaran M at Indian Institute of Sciences Bangalore, India for useful comments on the contents of manuscript. Author also wish to acknowledge the Science and Engineering Research Board under the Department of Science and Technology, New Delhi for granting the project associated (EEQ/2020/000480) with this work.

SUPPORTING INFORMATION

Force field parameters, Density calculation on varying number of molecules for ethaline system, Annealing information, Hydrogen bond labels, β parameter, Diffusivity fitted parameter and diffusion coefficient in the range 298 K–328 K

References

[1] S. Chen, Y. Zhao, B. Sun, Z. Ao, X. Xie, Y. Wei, G. Wang, Microwave-assisted synthesis of mesoporous co3o4 nanoflakes for applications in lithium ion batteries and oxygen evolution reactions, ACS Applied Materials & Interfaces 7 (5) (2015) 3306–3313, pMID: 25584769. arXiv:https://doi.org/10.1021/am508136k, doi:10.1021/am508136k.
URL https://doi.org/10.1021/am508136k

[2] C. Zhang, N. Mahmood, H. Yin, F. Liu, Y. Hou, Synthesis of phosphorus-doped graphene and its multifunctional applications for oxygen reduction reaction and lithium ion batteries, Advanced Materials 25 (35) (2013) 4932–4937. arXiv:https://onlinelibrary.wiley.com/doi/pdf/10.1002/adma.201301870, doi:https://doi.org/10.1002/adma.201301870.
URL https://onlinelibrary.wiley.com/doi/abs/10.1002/adma.201301870

[3] Q. Li, Y. Wu, Z. Wang, H. Ming, W. Wang, D. Yin, L. Wang, H. N. Alshareef, J. Ming, Carbon nanotubes coupled with metal ion diffusion layers stabilize oxide conversion reactions in high-voltage lithium-ion batteries, ACS Applied Materials & Interfaces 12 (14) (2020) 16276–16285, pMID: 32167290. arXiv:https://doi.org/10.1021/acsami.9b22175, doi:10.1021/acsami.9b22175.
URL https://doi.org/10.1021/acsami.9b22175

[4] A. M. Haregewoin, A. S. Wotango, B.-J. Hwang, Electrolyte additives for lithium ion battery electrodes: progress and perspectives, Energy Environ. Sci. 9 (2016) 1955–1988. doi:10.1039/C6EE00123H.
URL http://dx.doi.org/10.1039/C6EE00123H

[5] Y. Yamada, K. Furukawa, K. Sodeyama, K. Kikuchi, M. Yaegashi, Y. Tateyama, A. Yamada, Unusual stability of acetonitrile-based superconcentrated electrolytes for fast-charging lithium-ion batteries, Journal of the American Chemical Society 136 (13) (2014) 5039–5046, pMID: 24654781. arXiv:https://doi.org/10.1021/ja412807w, doi:10.1021/ja412807w.
URL https://doi.org/10.1021/ja412807w

[6] S. S. Zhang, A review on electrolyte additives for lithium-ion batteries, Journal of Power Sources 162 (2) (2006) 1379 – 1394, special issue including selected papers from the International Power Sources Symposium 2005 together with regular papers.

425 doi:https://doi.org/10.1016/j.jpowsour.2006.07.074.
426 URL http://www.sciencedirect.com/science/article/pii/
427 S0378775306017538

428 [7] J. C. Bachman, S. Muy, A. Grimaud, H.-H. Chang, N. Pour, S. F. Lux,
429 O. Paschos, F. Maglia, S. Lupart, P. Lamp, L. Giordano, Y. Shao-Horn,
430 Inorganic solid-state electrolytes for lithium batteries: Mechanisms and
431 properties governing ion conduction, Chemical Reviews 116 (1) (2016) 140–
432 162, pMID: 26713396. arXiv:https://doi.org/10.1021/acs.chemrev.
433 5b00563, doi:10.1021/acs.chemrev.5b00563.
434 URL https://doi.org/10.1021/acs.chemrev.5b00563

435 [8] Z. Xue, D. He, X. Xie, Poly(ethylene oxide)-based electrolytes for lithium-
436 ion batteries, J. Mater. Chem. A 3 (2015) 19218–19253. doi:10.1039/
437 C5TA03471J.
438 URL http://dx.doi.org/10.1039/C5TA03471J

439 [9] Z. Xue, D. He, X. Xie, Poly(ethylene oxide)-based electrolytes for lithium-
440 ion batteries, J. Mater. Chem. A 3 (2015) 19218–19253. doi:10.1039/
441 C5TA03471J.
442 URL http://dx.doi.org/10.1039/C5TA03471J

443 [10] K. Leung, J. L. Budzien, Ab initio molecular dynamics simulations of the
444 initial stages of solid–electrolyte interphase formation on lithium ion bat-
445 tery graphitic anodes, Phys. Chem. Chem. Phys. 12 (2010) 6583–6586.
446 doi:10.1039/B925853A.
447 URL http://dx.doi.org/10.1039/B925853A

448 [11] J. C. Bachman, S. Muy, A. Grimaud, H.-H. Chang, N. Pour, S. F. Lux,
449 O. Paschos, F. Maglia, S. Lupart, P. Lamp, L. Giordano, Y. Shao-Horn,
450 Inorganic solid-state electrolytes for lithium batteries: Mechanisms and
451 properties governing ion conduction, Chemical Reviews 116 (1) (2016) 140–
452 162, pMID: 26713396. arXiv:https://doi.org/10.1021/acs.chemrev.

5b00563, doi:10.1021/acs.chemrev.5b00563.
URL https://doi.org/10.1021/acs.chemrev.5b00563

[12] M. Ishikawa, T. Sugimoto, M. Kikuta, E. Ishiko, M. Kono, Pure ionic liquid electrolytes compatible with a graphitized carbon negative electrode in rechargeable lithium-ion batteries, Journal of Power Sources 162 (1) (2006) 658 – 662. doi:https://doi.org/10.1016/j.jpowsour.2006.02.077.
URL http://www.sciencedirect.com/science/article/pii/S0378775306004034

[13] V. Chakrapani, F. Rusli, M. A. Filler, P. A. Kohl, Quaternary ammonium ionic liquid electrolyte for a silicon nanowire-based lithium ion battery, The Journal of Physical Chemistry C 115 (44) (2011) 22048–22053. arXiv:https://doi.org/10.1021/jp207605w, doi:10.1021/jp207605w.
URL https://doi.org/10.1021/jp207605w

[14] A. P. Abbott, D. Boothby, G. Capper, D. L. Davies, R. K. Rasheed, Deep eutectic solvents formed between choline chloride and carboxylic acids: versatile alternatives to ionic liquids, Journal of the American Chemical Society 126 (29) (2004) 9142–9147, pMID: 15264850. arXiv:https://doi.org/10.1021/ja048266j, doi:10.1021/ja048266j.
URL https://doi.org/10.1021/ja048266j

[15] C. A. Nkuku, R. J. LeSuer, Electrochemistry in deep eutectic solvents, The Journal of Physical Chemistry B 111 (46) (2007) 13271–13277, pMID: 17973421. arXiv:https://doi.org/10.1021/jp075794j, doi:10.1021/jp075794j.
URL https://doi.org/10.1021/jp075794j

[16] C. D'Agostino, R. C. Harris, A. P. Abbott, L. F. Gladden, M. D. Mantle, Molecular motion and ion diffusion in choline chloride based deep eutectic solvents studied by 1h pulsed field gradient nmr spectroscopy, Phys. Chem. Chem. Phys. 13 (2011) 21383–21391. doi:10.1039/C1CP22554E.
URL http://dx.doi.org/10.1039/C1CP22554E

[17] C. Florindo, F. S. Oliveira, L. P. N. Rebelo, A. M. Fernandes, I. M. Marrucho, Insights into the synthesis and properties of deep eutectic solvents based on cholinium chloride and carboxylic acids, ACS Sustainable Chemistry & Engineering 2 (10) (2014) 2416–2425. arXiv:https://doi.org/10.1021/sc500439w, doi:10.1021/sc500439w.
URL https://doi.org/10.1021/sc500439w

[18] H.-R. Jhong, D. S.-H. Wong, C.-C. Wan, Y.-Y. Wang, T.-C. Wei, A novel deep eutectic solvent-based ionic liquid used as electrolyte for dye-sensitized solar cells, Electrochemistry Communications 11 (1) (2009) 209 – 211. doi:https://doi.org/10.1016/j.elecom.2008.11.001.
URL http://www.sciencedirect.com/science/article/pii/S1388248108005249

[19] A. P. Abbott, G. Capper, D. L. Davies, K. J. McKenzie, S. U. Obi, Solubility of metal oxides in deep eutectic solvents based on choline chloride, Journal of Chemical & Engineering Data 51 (4) (2006) 1280–1282. arXiv:https://doi.org/10.1021/je060038c, doi:10.1021/je060038c.
URL https://doi.org/10.1021/je060038c

[20] P. Cen, K. Spahiu, M. S. Tyumentsev, M. R. S. J. Foreman, Metal extraction from a deep eutectic solvent, an insight into activities, Phys. Chem. Chem. Phys. 22 (2020) 11012–11024. doi:10.1039/C9CP05982B.
URL http://dx.doi.org/10.1039/C9CP05982B

[21] A. Söldner, J. Zach, B. König, Deep eutectic solvents as extraction media for metal salts and oxides exemplarily shown for phosphates from incinerated sewage sludge ash, Green Chem. 21 (2019) 321–328. doi:10.1039/C8GC02702A.
URL http://dx.doi.org/10.1039/C8GC02702A

[22] A. S. L. Gouveia, F. S. Oliveira, K. A. Kurnia, I. M. Marrucho, Deep eutectic solvents as azeotrope breakers: Liquid–liquid extraction and cosmo-rs prediction, ACS Sustainable Chemistry & Engineering 4 (10) (2016)

5640–5650. arXiv:https://doi.org/10.1021/acssuschemeng.6b01542, doi:10.1021/acssuschemeng.6b01542.
URL https://doi.org/10.1021/acssuschemeng.6b01542

[23] F. Pena-Pereira, J. Namieśnik, Ionic liquids and deep eutectic mixtures: Sustainable solvents for extraction processes, ChemSusChem 7 (7) (2014) 1784–1800. arXiv:https://chemistry-europe.onlinelibrary.wiley.com/doi/pdf/10.1002/cssc.201301192, doi:https://doi.org/10.1002/cssc.201301192.
URL https://chemistry-europe.onlinelibrary.wiley.com/doi/abs/10.1002/cssc.201301192

[24] N. R. Mirza, N. J. Nicholas, Y. Wu, K. A. Mumford, S. E. Kentish, G. W. Stevens, Experiments and thermodynamic modeling of the solubility of carbon dioxide in three different deep eutectic solvents (dess), Journal of Chemical & Engineering Data 60 (11) (2015) 3246–3252. arXiv:https://doi.org/10.1021/acs.jced.5b00492, doi:10.1021/acs.jced.5b00492.
URL https://doi.org/10.1021/acs.jced.5b00492

[25] G. García, S. Aparicio, R. Ullah, M. Atilhan, Deep eutectic solvents: Physicochemical properties and gas separation applications, Energy & Fuels 29 (4) (2015) 2616–2644. arXiv:https://doi.org/10.1021/ef5028873, doi:10.1021/ef5028873.
URL https://doi.org/10.1021/ef5028873

[26] M. W. Nam, J. Zhao, M. S. Lee, J. H. Jeong, J. Lee, Enhanced extraction of bioactive natural products using tailor-made deep eutectic solvents: application to flavonoid extraction from flos sophorae, Green Chem. 17 (2015) 1718–1727. doi:10.1039/C4GC01556H.
URL http://dx.doi.org/10.1039/C4GC01556H

[27] A. Boisset, J. Jacquemin, M. Anouti, Physical properties of a new deep eutectic solvent based on lithium bis[(trifluoromethyl)sulfonyl]imide and

n-methylacetamide as superionic suitable electrolyte for lithium ion batteries and electric double layer capacitors, Electrochimica Acta 102 (2013) 120 – 126. doi:https://doi.org/10.1016/j.electacta.2013.03.150.
URL http://www.sciencedirect.com/science/article/pii/S0013468613005732

[28] A. Boisset, S. Menne, J. Jacquemin, A. Balducci, M. Anouti, Deep eutectic solvents based on n-methylacetamide and a lithium salt as suitable electrolytes for lithium-ion batteries, Phys. Chem. Chem. Phys. 15 (2013) 20054–20063. doi:10.1039/C3CP53406E.
URL http://dx.doi.org/10.1039/C3CP53406E

[29] L. Millia, V. Dall'Asta, C. Ferrara, V. Berbenni, E. Quartarone, F. M. Perna, V. Capriati, P. Mustarelli, Bio-inspired choline chloride-based deep eutectic solvents as electrolytes for lithium-ion batteries, Solid State Ionics 323 (2018) 44 – 48. doi:https://doi.org/10.1016/j.ssi.2018.05.016.
URL http://www.sciencedirect.com/science/article/pii/S0167273817305295

[30] W. L. Jorgensen, D. S. Maxwell, J. Tirado-Rives, Development and testing of the opls all-atom force field on conformational energetics and properties of organic liquids, Journal of the American Chemical Society 118 (45) (1996) 11225–11236. arXiv:https://doi.org/10.1021/ja9621760, doi:10.1021/ja9621760.
URL https://doi.org/10.1021/ja9621760

[31] B. Doherty, O. Acevedo, Opls force field for choline chloride-based deep eutectic solvents, The Journal of Physical Chemistry B 122 (43) (2018) 9982–9993, pMID: 30125108. arXiv:https://doi.org/10.1021/acs.jpcb.8b06647, doi:10.1021/acs.jpcb.8b06647.
URL https://doi.org/10.1021/acs.jpcb.8b06647

[32] S. L. Perkins, P. Painter, C. M. Colina, Experimental and computational studies of choline chloride-based deep eutectic solvents, Journal of Chemical

& Engineering Data 59 (11) (2014) 3652–3662. arXiv:https://doi.org/10.1021/je500520h, doi:10.1021/je500520h.
URL https://doi.org/10.1021/je500520h

[33] J. M. Vicent-Luna, J. Idígoras, S. Hamad, S. Calero, J. A. Anta, Ion transport in electrolytes for dye-sensitized solar cells: A combined experimental and theoretical study, The Journal of Physical Chemistry C 118 (49) (2014) 28448–28455. arXiv:https://doi.org/10.1021/jp509193h, doi:10.1021/jp509193h.
URL https://doi.org/10.1021/jp509193h

[34] J. qvist, Ion-water interaction potentials derived from free energy perturbation simulations, The Journal of Physical Chemistry 94 (21) (1990) 8021–8024. arXiv:https://doi.org/10.1021/j100384a009, doi:10.1021/j100384a009.
URL https://doi.org/10.1021/j100384a009

[35] M. J. Abraham, T. Murtola, R. Schulz, S. Páll, J. C. Smith, B. Hess, E. Lindahl, Gromacs: High performance molecular simulations through multi-level parallelism from laptops to supercomputers, SoftwareX 1-2 (2015) 19 – 25. doi:https://doi.org/10.1016/j.softx.2015.06.001.
URL http://www.sciencedirect.com/science/article/pii/S2352711015000059

[36] L. Martínez, R. Andrade, E. G. Birgin, J. M. Martínez, Packmol: A package for building initial configurations for molecular dynamics simulations, Journal of Computational Chemistry 30 (13) (2009) 2157–2164. arXiv:https://onlinelibrary.wiley.com/doi/pdf/10.1002/jcc.21224, doi:https://doi.org/10.1002/jcc.21224.
URL https://onlinelibrary.wiley.com/doi/abs/10.1002/jcc.21224

[37] H. G. Petersen, Accuracy and efficiency of the particle mesh ewald method, The Journal of Chemical Physics 103 (9) (1995) 3668–3679. arXiv:https:

//doi.org/10.1063/1.470043, doi:10.1063/1.470043.
URL https://doi.org/10.1063/1.470043

[38] G. Bussi, D. Donadio, M. Parrinello, Canonical sampling through velocity rescaling, The Journal of Chemical Physics 126 (1) (2007) 014101. arXiv:https://doi.org/10.1063/1.2408420, doi:10.1063/1.2408420.
URL https://doi.org/10.1063/1.2408420

[39] H. J. C. Berendsen, J. P. M. Postma, W. F. van Gunsteren, A. DiNola, J. R. Haak, Molecular dynamics with coupling to an external bath, The Journal of Chemical Physics 81 (8) (1984) 3684–3690. arXiv:https://doi.org/10.1063/1.448118, doi:10.1063/1.448118.
URL https://doi.org/10.1063/1.448118

[40] W. Humphrey, A. Dalke, K. Schulten, VMD – Visual Molecular Dynamics, Journal of Molecular Graphics 14 (1996) 33–38.